RESEARCH ARTICLE

ADVANCED OPTICAL MATERIALS
www.advopticalmat.de

Broadband Complete Polarization Control via Inverse-Designed Photonic Crystal Slabs

Ruhuan Deng, Xinhao Wang, Yi Zuo, Zhen Liu, Feifan Wang, Chao Peng, Tongyu Li, Wenzhe Liu,* Xiaohan Liu, and Lei Shi**

Polarization is a crucial characteristic of electromagnetic fields, and the ability to fully control it has many useful applications. While novel nanophotonic devices have been designed to achieve unprecedented capability to manipulate light on demand, their usage in the complete control of polarization states for the transmitted light has been relatively limited, and traditional design methods always produce devices with narrow operation bandwidths. In this work, a two-phase topology optimization strategy is proposed in conjunction with adjoint method to inverse design photonic crystal slabs capable of complete polarization control. It successfully produces devices operating over a broad bandwidth that is significantly larger than the current state-of-the-art designs, and their performances are also robust to material loss. This is also find that the C_{2v} symmetry of the structure can regularize the problem, so that less simulation time and faster convergence can be obtained without compromising performance. This study demonstrates the power of the inverse design method, which can be further applied to achieve more complex polarization control and beyond.

1. Introduction

As a very important and unique property of electromagnetic waves, polarization underpins a wide range of photonic technologies for optical communication,[1] spectroscopy,[2] and biomedical imaging.[3] Conventionally, polarization control is achieved using wave plates and polarizers, which mainly rely on their materials' properties like anisotropy. Nowadays, nanophotonic devices such as photonic crystal slabs[4–6] and metasurfaces[7–9] offer new avenues for tailoring electromagnetic waves' polarization. They are capable of realizing various functionalities with unprecedented performance, for example, Yu Guo et al.[10] achieved complete polarization conversion for reflected light using photonic crystal slabs, which is topologically protected; Virginie Lousse et al.[11] designed a photonic crystal slab that can selectively reflect and transmit electromagnetic waves depending on its polarization by reducing the structure's rotational symmetry; Sergey Kruk et al.[7] used metasurfaces to control polarization utilizing the generalized Huygens principle, and demonstrated high efficiency half-wave plates, quarter-wave plates and vector beam q-plates. Importantly, these nanophotonic devices rely on its sub-wavelength nanostructures to manipulate the polarization of electromagnetic waves. This allows them to achieve compact footprints, broad design flexibility, and precise control-attributes that are essential for both fundamental research and practical applications.

Intuition-based approaches are frequently applied to design nanophotonic devices, where geometry structures are inspired

R. Deng, X. Wang, T. Li, X. Liu, L. Shi
State Key Laboratory of Surface Physics
Key Laboratory of Micro- and Nano-Photonic Structures (Ministry of Education) and Department of Physics
Fudan University
Shanghai 200433, China
E-mail: lity18@fudan.edu.cn; lshi@fudan.edu.cn

Y. Zuo, Z. Liu[+], F. Wang, C. Peng
State Key Laboratory of Advanced Optical Communication Systems and Networks, Department of Electronics & Frontiers Science Center for Nano-optoelectronics
Peking University
Beijing 100871, China

W. Liu, L. Shi
State Key Laboratory of Surface Physics
Institute for Nanoelectronic Devices and Quantum Computing
Fudan University
Shanghai 200438, China
E-mail: wzliu15@fudan.edu.cn

X. Liu, L. Shi
Collaborative Innovation Center of Advanced Microstructures
Nanjing University
Nanjing 210093, China

L. Shi
Shanghai Research Center for Quantum Sciense
Shanghai 201315, China

The ORCID identification number(s) for the author(s) of this article can be found under https://doi.org/10.1002/adom.202303218

[+]Present address: Department of Electrical and Computer Engineering, Boston university, Boston 02215, USA

DOI: 10.1002/adom.202303218

by prior physics knowledge and the specific parameters are fine tuned to achieve expected performance. Lately, along with breakthroughs in computer science, a new design strategy called inverse design was rapidly developed. Powered by effective algorithms including adjoint optimization,[12–14] machine learning[15,16] and convex optimization,[17,18] inverse design methods automatically optimize devices' geometries to satisfy user-defined objectives. Furthermore, they can always lead to high performance devices with nonintuitive patterns. Unlike conventional intuitive strategies, inverse design is not limited by people's intuition, and thus can fully exploit the design space, potentially delivering structures with improved performance and unanticipated properties. Moreover, inverse design is highly automated and efficient. It is increasingly used in designing nanophotonic devices: Wei Ma et al.[19] utilized machine-learning models to inverse design multifunctional metasurfaces, implementing polarization-multiplexed multicolor holograms; Zin Lin et al.[20] introduced an end-to-end inverse design method for metasurfaces, and achieved multi-channel imaging; F. Callewaert et al.[21] used an objective-first algorithm to inverse design high efficiency metasurface polarization beamsplitters. While these works have taken polarization into consideration, few have focused on the modulation of the polarization states of electromagnetic waves, especially in photonic crystal slab devices. Furthermore, polarization-control nanophotonic devices designed by conventional methods typically operate only at specific wavelengths or in a narrow spectral range.[7]

In this paper, through an adjoint-based inverse-design approach, we develop photonic crystal slabs capable of achieving complete polarization control at normal incidence with a high efficiency (average 85%). At the same time, its operational bandwidth (1300 nm to 1540 nm) is nearly two times as large as pervious polarization control devices based on nanophotonics.[7] Without adding any physical knowledge in advance, the initial structure automatically evolves into a stripe-like structure. In addition, it has many fine features to compensate for the dispersion and achieve broadband performance. Inspired by the optimized structures, we further consider the effect of geometric symmetry on our optimization problem. It is found that by appropriately setting the constraint on structural symmetry, the optimization process can be sped up. Also, competent results can be obtained even when the degrees of freedom shrank due to the symmetry. It indicates that co-polarization is preferable to achieve complete polarization control, and geometric symmetry can be used as a good regularization.

2. Experimental Section

The inverse design approach achieves complete polarization control by realizing large meridian coverage on the Poincaré sphere. Complete polarization control means the polarization state of the output light can cover the whole Poincaré sphere (from a practical point of view, the normal incidence case was consider). This problem was simplify to covering a single meridian on the Poincaré sphere. Considering a linearly polarized input, The output light would like to achieve the meridian coverage by optimizing and designing the geometric structure of the photonic crystal slab's unit cell. The output polarization passing through the structure was expected to traverse all polarization ellipses with a fixed principal axis direction while individually rotating the input polarization direction, as shown in **Figure 1a**.

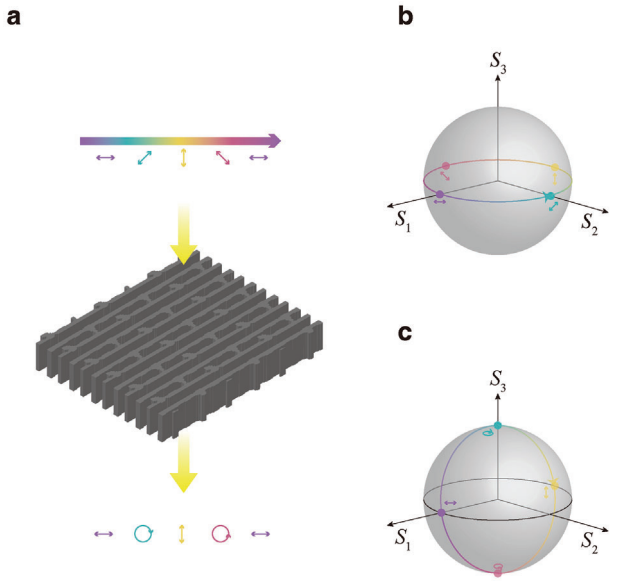

Figure 1. The design target of the photonic crystal slab. a) The illustration of the polarization-control photonic crystal slab. Different linearly polarized light, normally incident on the designed device, transmit with complete polarization states. b) The polarization states' trajectory of input light on the Poincaré sphere; S_1, S_2,and S_3 were the first, second, and third Stokes parameters, respectively. c) The polarization states' trajectory of output light on the Poincaré sphere.

Specifically, the polarization state's evolution was illustrated on the Poincaré sphere. For the incident light, its polarization state's trajectory was shown in Figure 1b. While its polarization direction was rotated, its polarization state will move continuously and fully cover the equator ($S_3 = 0$) on the Poincaré sphere. After the polarization conversion by the designed photonic crystal slab, the output polarization state should correspondingly cover the meridian ($S_2 = 0$) as shown in Figure 1c. The output polarization will gradually change with the input polarization direction. It transforms sequentially from linearly horizontal polarization to right circularly polarization ($S_3 = 1$), linearly vertical polarization, left circularly polarization ($S_3 = -1$), and finally back to the linearly horizontal polarization. Having the $S_2 = 0$ meridian covered, all the other meridians can then be covered by rotating the whole system synchronously.

The optimization method used was topology optimization based on adjoint method. Topology optimization[22] was an approach that represents the optimized structure in pixels. Usually, each pixel takes a design variable ρ called material density that was either 0 (void) or 1 (solid), and they can change continuously during the optimization to enable gradient-based optimization. The pixel size were set to 20 nm × 20 nm here for a balance between the degree of freedom, simulation accuracy and simulation time. As we were optimizing photonic crystal slabs, the structure was then represented by a 2D gray-scale bitmap as shown in Figure 1c. The mapping from design variables ρ to material properties ϵ (for the case) was called material interpolation. There were different strategies for different purposes, and the filtering-threshold scheme was adopted for further discretization of de-

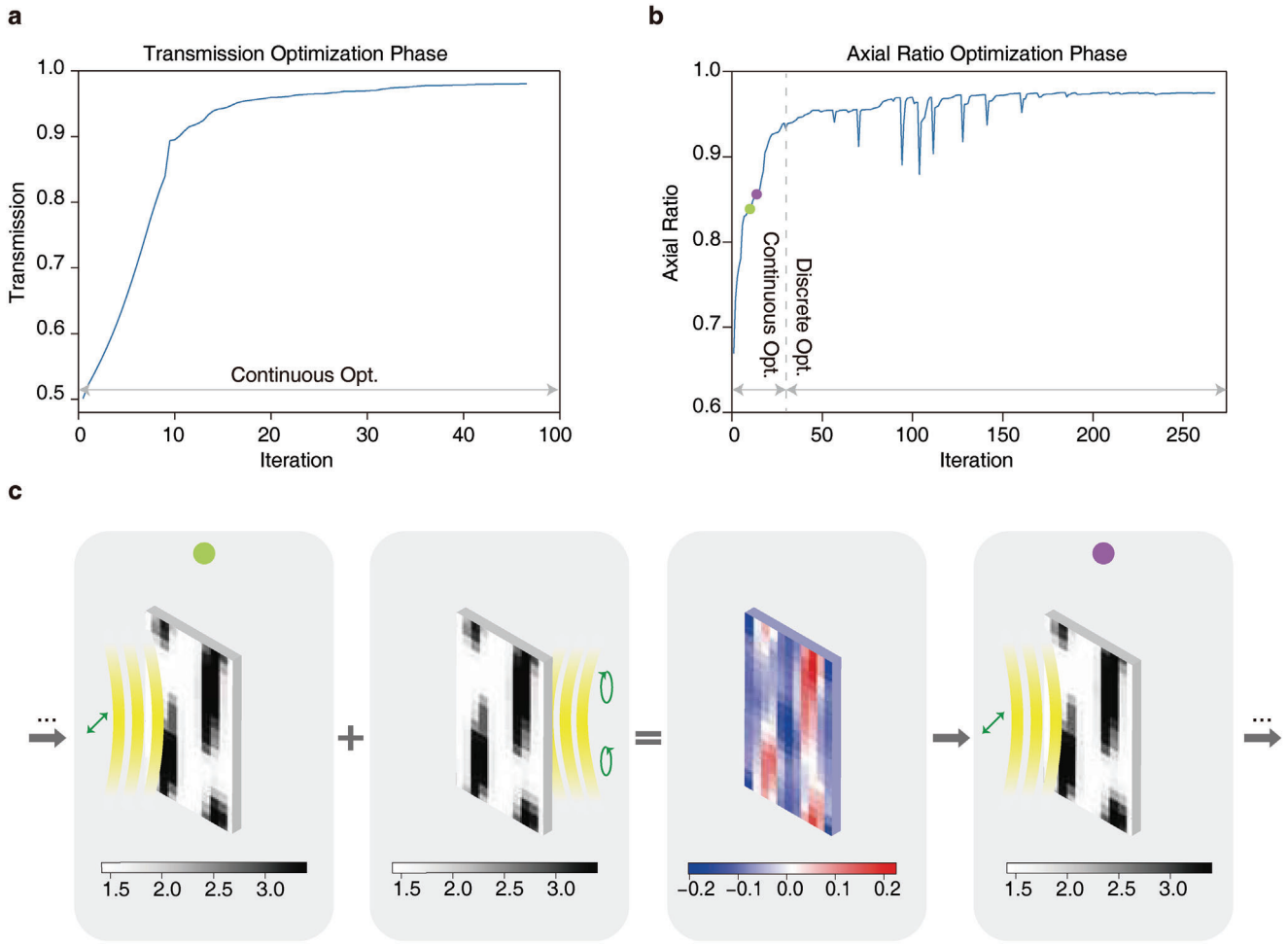

Figure 2. The description of the design process. a) The objective value at each iteration in the first optimization phase, with transmission as the FoM. b) The objective value at each iteration in the second optimization phase, with axial ratio as the FoM. The dotted vertical line indicates transition from continuous optimization to discrete optimization. c) The illustration of one optimization step labeled in (b) with green and purple dots.

signed structures. The detailed implementation of this scheme can be found in Section S1 of the Supporting Information. Topology optimization explores the full design space and can thus lead to devices with better performances. While it provides thousands of degrees of freedom for optimizations, calculating the gradient of figure of merit (FoM) with respect to these design variables can be computationally expensive. For example, in direct differentiation, thousands of simulations (as many as the number of design variables) should be run to obtain the gradient for each iteration, and it was impractical for many problems. However utilizing the Lorentz reciprocity, adjoint method[23] can efficiently calculate the gradient. Regardless of the number of design variables, it only needs two simulations to obtain the gradient. A detailed derivation of it can be found in Section S2 of the Supporting Information. With the gradient information, the structure was iteratively optimize of photonic crystal slabs using the L-BFGS-B[24] algorithm to achieve satisfactory results.

The process of each iteration was shown in **Figure** 2c. First, in the forward simulations, linearly polarized light was shined normally on the photonic crystal slab being optimized. This gives the field distributions and the FoM. Then in the adjoint simulations, circularly polarized light was normally shined on the optimized structure from the original transmitting direction so that the corresponding field distributions were obtained. Combining the field distributions from forward and adjoint simulations, the gradient field was calculated using adjoint method and update the photonic crystal slab's geometry with the gradient, starting the next iteration.

In addition to the complete polarization control, the objectives also include high transmission efficiency for practical application. However, simply optimize these two objectives simultaneously do not provide satisfactory results. The optimization process can easily get trapped in the middle due to the competition between these two objectives (more details can be found in Section S3 of the Supporting Information). Notice that the main target was the complete polarization control, and the requirement of high transmission efficiency can be moderately relaxed. Therefore, a two-phase optimization strategy was designed. The first phase was the transmission optimization phase, which aims to improve the transmission efficiency. During this phase, transmission amplitude was set as the FoM. The material densities were continuous variables constructed under a filtering-

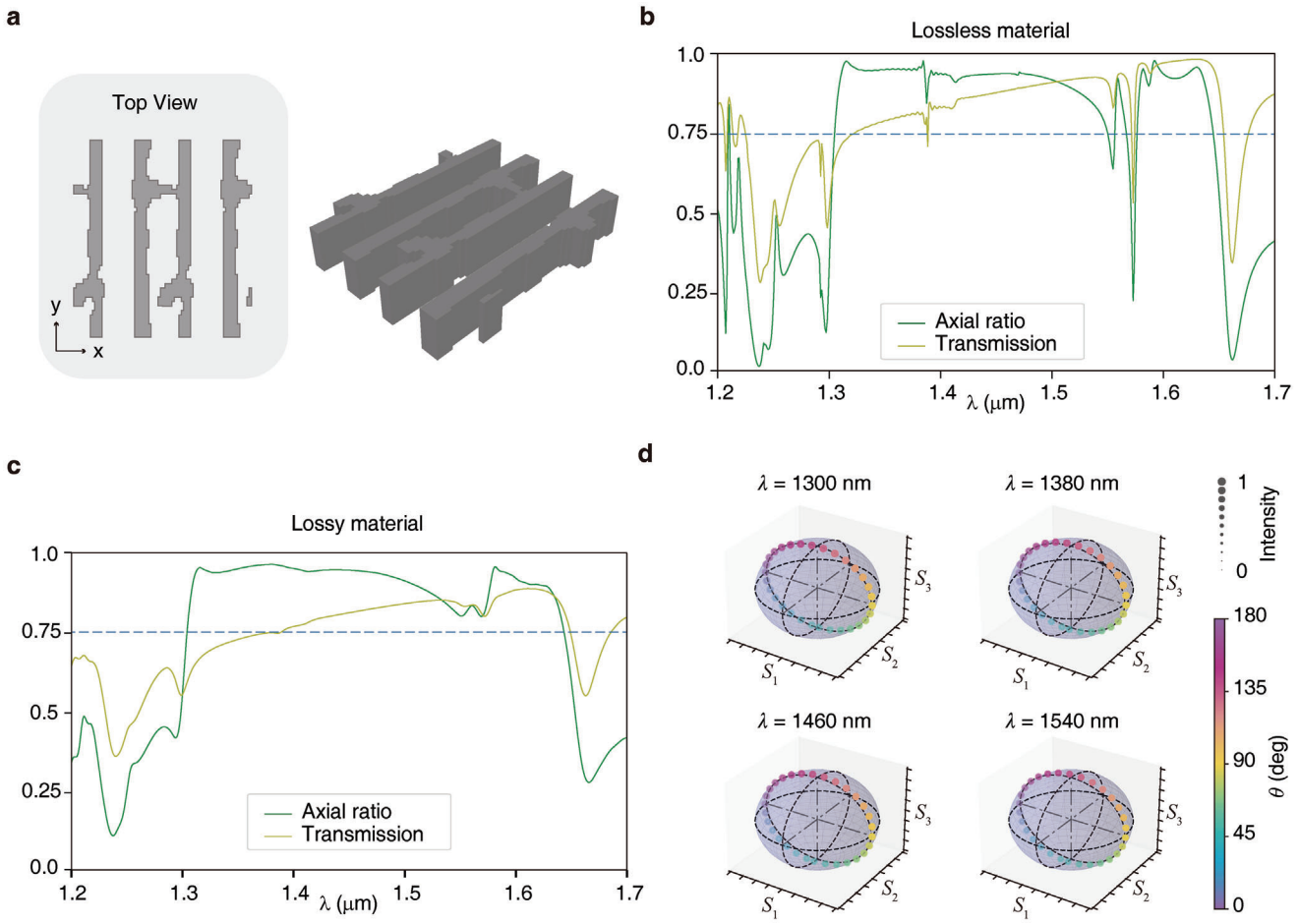

Figure 3. Results of our inverse designed photonic crystal slab. a) Geometry structure of the designed polarizarion-control photonic crystal slab. c) Transmission and axial ratio spectra of the designed device with input light 45 degree linearly polarized for lossy material b) Transmission and axial ratio spectra of the designed device with input light 45 degree linearly polarized for lossless material. d) Polarization states' trajectories of output light on the Poincaré sphere at four wavelengths. The color of points on trajectories indicate the polarization direction of input linearly polarized light, and the size of points indicate the intensity of output light.

threshold scheme.[25,26] The parameter β in the threshold step was fixed at a small value to enable free evolution of the variables, which was call continuous optimization. The objective value at each iteration was shown in Figure 2a. The second phase was the axial ratio optimization phase, where the axial ratio was set as the FoM and the coverage of the output polarization state was tried to improve. After the continuous optimization, the discrete optimization was conducted by gradually increasing the parameter β to "push" material densities to 0 or 1, and ultimately produced discrete structures which were manufacturable. The evolution of the objective value in this phase was shown in Figure 2b.

3. Results

To achieve the broadband performance, we set the wavelength range of our optimization to 1300–1500 nm, which is significantly larger that the best broadband complete-polarization-control device based on nanophotonics to date. We evenly sample the data points in this range, and construct the overall FoM by taking the average of the sampled FoM as $\mathrm{FoM} = \sum_{i=1}^{n} \mathrm{FoM}(\omega_i)/n$. Free-standing silicon (Si, refractive index $n \approx 3.51$) photonic crystal slabs are designed here with surrounding material set as oil (refractive index $n \approx 1.44$). The optimization starts with cylinders in a hexagonal lattice, and the thickness is fixed during the optimization. We randomly generate initial structures with various thicknesses and radii, and find the best result from cylinders with 180 nm radius and 690 nm thickness. We arrive at a fully discrete structure after two phases of the optimization, as shown in **Figure 3**a. The transmission and the axial ratio spectra of the transmitted light at normal incidence are shown in Figure 3b. By the convention that axial ratio of the circularly polarized light should exceed 0.75 to experimentally perform well, the usable wavelength bandwidth of the optimized device reaches 240 nm (1300–1540 nm). It is almost twice as large as the best one designed by an intuition-based approach,[7] and the average transmission is as high as 85% in this range. Also notice that the material is not ideally lossless in the experiment, and the inclusion of a loss term might deteriorate the performance of the device, so we further examine the effect of material loss for our design. We add an imaginary part of $0.01i$ to the refractive index and re-

calculate the transmission and the axial ratio spectra as plotted in Figure 3c. It shows that the wavelength range that meets the requirement is not shortened but broadened to 340 nm (1300–1640 nm), as the sharp resonant peaks are flattened, and the overall transmission only decreases about 7%. This demonstrates the robustness of our design toward material loss. A detailed discussion about material loss's impact on our designed structure can be found in Section S4 of the Supporting Information.

It is worth noting that we do not add any prior knowledge during the optimization. This is an important advantage of inverse design, because the result will not be limited by designers. Moreover, it can always produce devices with high performance and inspiring structures, which in turn improve our understanding to the underlying physics. In our case, we find that the structure automatically evolves into a stripe-like shape. This is intuitively reasonable, as this structure can induce anisotropy for the x- and y- polarized light, thus enabling polarization conversion. Also, the optimized structure has many fine features. They enable the wide operational bandwidth because they compensate for the chromatic dispersion, which can spoil the performance of polarization conversion. And this is a difficult part to overcome with traditional design methods, as limitations of both designers and computational resources constrain the complexity of the structure. To illustrate it, we provide a detailed comparison between the performance of our optimized structure and the stripe structure in Section S5 of the Supporting Information.

For better visualization of the results, the trajectory of the transmitted light's polarization states on the Poincaré sphere are shown in Figure 3d. We display the trajectories for different wavelengths and characterize the transmitted light with points of different colors and sizes. The color of these points reflects the polarization direction of the incident linearly polarized light, and the size of the points reflects the transmission efficiency. As seen from the point sizes, the transmittance is very high (above 70%) in all cases (different wavelengths and polarization directions of the incident light). It is shown that at all wavelengths, the output polarization states can fully cover the meridian ($S_2 = 0$) as our design target. We also notice that when the input light is x- or y-polarized (purple or yellow), the output polarization states lie on $S_1 = 1$ (x-polarized) and $S_1 = -1$ (y-polarized) respectively. This means that cross-polarization is almost non-existent here, and it is also supported by the final structure. Not imposing any symmetry during the optimization, it automatically evolves to the geometry that tends to have C_{2v} symmetry. Under normal incidence, this structure forbids TE and TM modes' cross-polarization, which implies that co-polarization is sufficient to achieve broadband complete polarization control.

In order to verify our assumption, we consider the structure possessing C_{2v} symmetry as shown in **Figure** 4a. The number of design parameters is reduced to a quarter by only considering the upper right portion of the structure, the smallest irreducible asymmetric unit. During the optimization, the geometry in the simulation is constructed by unfolding the smallest unit according to symmetry operations of the C_{2v} group. Then after performing the forward and adjoint simulation, gradients with respect to the complete structure are calculated through adjoint method. We then fold these into the smallest unit to produce gradients with respect to the design variables that we will eventually use in the optimization. Optimizations start from the same initial structures, cylinders in a square lattice, with various thicknesses and radii. We optimize the transmission efficiency for both asymmetric structures and C_{2v}*text* − *symmetric* structures, and results are plotted in Figure 4b. The colors of scatters indicate the transmission of optimized structures, and the coordinates show the radius and thickness of the initial structure. It shows structures with forced C_{2v} symmetry perform equally well as the asymmetric ones. This indicates the extra degrees of freedom from asymmetry do not significantly improve polarization control capability here. Thus, we only need to consider the C_{2v}*text* − *symmetric* structure which forbids cross-polarization under normal incidence.

This simplification reduces the computational time. For example, in FDTD (Finite Difference Time Domain), simulations for x- and y- polarized incident light are 4 times faster. Those polarizations can be used to construct incident light with arbitrary polarization states. Besides, the average number of iterations for convergence decreases by almost 20% (from 17 to 13.5). This also suggests that imposing C_{2v} symmetry regularization to the structure is beneficial for the problem here. As a demonstration, we follow the same optimization routine for the C_{2v}*text* − *symmetric* geometry, and obtain an optimized structure as shown in Figure 4c. The transmission and the axial ratio spectra are plotted in Figure 4d with a usable wavelength range of 234 nm (1293–1527 nm), which is as good as the result with the asymmetric structure.

4. Conclusion

In summary, we propose a two-phase topology optimization strategy using adjoint method, and successfully optimize photonic crystals that enable high-efficiency complete polarization control in the largest wavelength range, to the best of our knowledge. We verify the robustness of our designed structure against material loss, and it turns out that the usable wavelength range is not decreased but rather increased owing to the suppression of resonances. While not imposing symmetry, the optimized structure automatically evolves into a stripe-like geometry that tends to have C_{2v} symmetry. Inspired by this phenomenon, we discuss the effect of imposing structural symmetry on the optimization and find that C_{2v}*text* − *symmetric* structures can provide a good regularization to our problem by allowing only co-polarization for TE and TM modes. While our discussion is limited to the normal-incidence case, we envision that this method can be applied for more complex inclined situations, and geometrical constraints can be used to make the designed structure easier to fabricate. Moreover, as the adjoint method is general for any polarization, the proposed method can be applied to other polarization control devices.

5. Computational Detail

FDTD method is used to perform forward and adjoint simulations, and the simulated fields are extracted and postprocessed using Python. Periodic boundary condition is used to simulate the photonic crystal, and the Fourier transform is used to obtain electromagnetic fields at multiple wavelengths through a single time domain simulation. As both forward and adjoint simula-

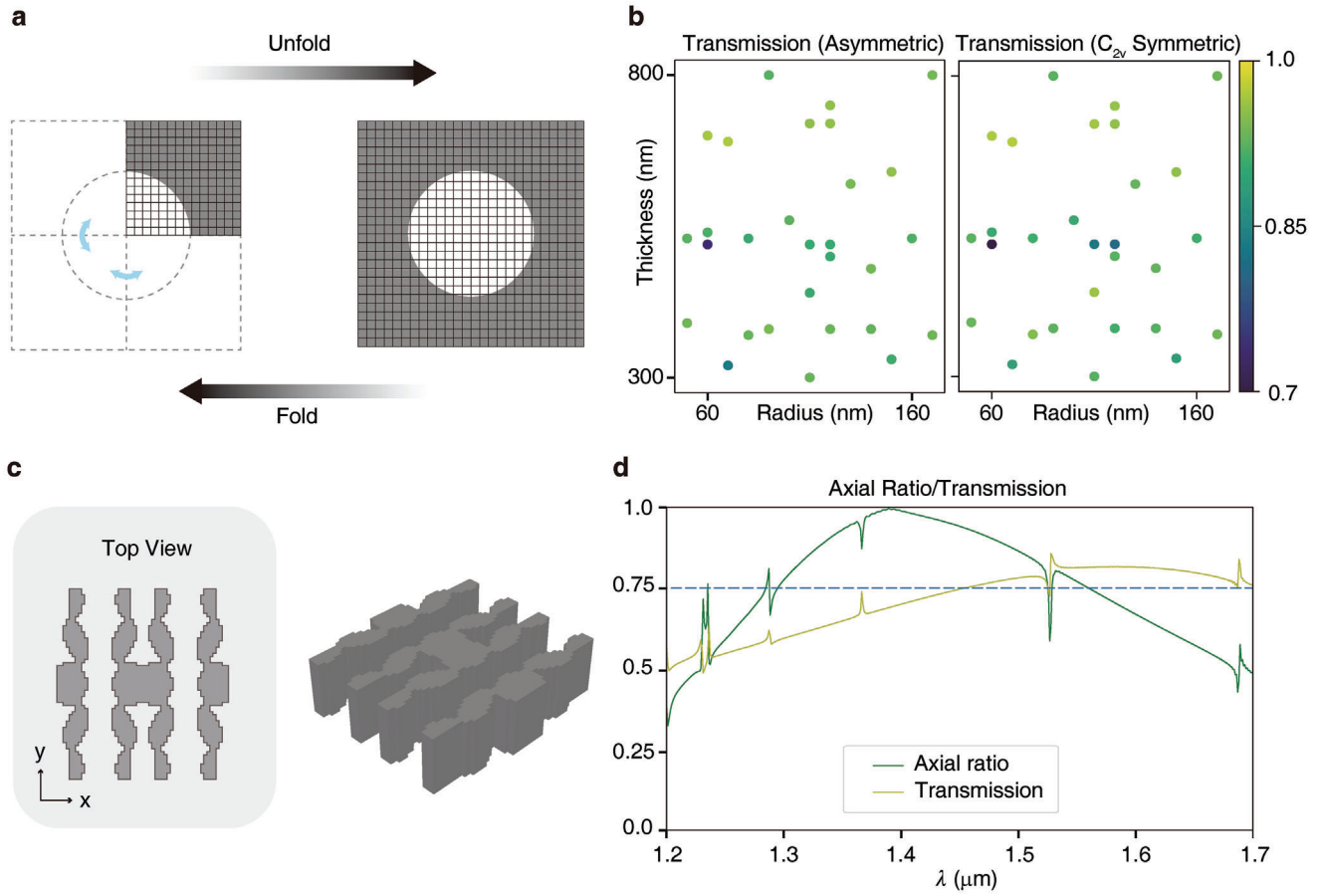

Figure 4. The process and results of optimization with symmetric geometry. a) The unfolding and folding process that impose symmetry. b) Distributions of the optimization results (transmission) with asymmetric and C_{2v} symmetric structures that start from the same initial geometries. The color of scatters indicates the transmission of the optimized structures. c) Geometry structure of the designed polarizarion-control photonic crystal slab with C_{2v} symmetry. d) Transmission and axial ratio spectra of the designed C_{2v} symmetric device with input light 45 degree linearly polarized.

tions require plane wave excitation at normal incidence with different polarization, we set two periodic/Bloch type plane wave sources with orthogonal polarizations to achieve arbitrary polarization. It is found that 1000 fs simulation time is enough for the simulation to converge. All computations are performed on our server (24-core CPU@3 GHz, 512 GB RAM). The optimization of the asymmetric structure takes 67 hours, and the optimization of the C2v-symmetric structure takes 35 hours.

Supporting Information

Supporting Information is available from the Wiley Online Library or from the author.

Acknowledgements

R.D. acknowledges useful comments and suggestions received from Dr. Jiajun Wang. This work was supported by National Natural Science Foundation of China (No. 12221004 and No. 12234007); National Key R&D Program of China (2022YFA1404800 and 2023YFA1406900); Major Program of National Natural Science Foundation of China (T2394481); Science and Technology Commission of Shanghai Municipality (22142200400, 21DZ1101500, 2019SHZDZX01 and 23DZ2260100).

Conflict of Interest

The authors declare no conflict of interest.

Data Availability Statement

The data that support the findings of this study are available from the corresponding author upon reasonable request.

Keywords

adjoint method, inverse design, photonic crystal

Received: December 18, 2023
Revised: March 12, 2024
Published online:

[1] Y. Han, G. Li, *Opt. Express* **2005**, *13*, 7527.
[2] C. Wieman, T. W. Hänsch, *Phys. Rev. Lett.* **1976**, *36*, 1170.
[3] L. Wang, D. Zimnyakov, in *Optical Polarization in Biomedical Applications*, Vol. *467*, Springer, Berlin, New York **2006**.

[4] W. Liu, B. Wang, Y. Zhang, J. Wang, M. Zhao, F. Guan, X. Liu, L. Shi, J. Zi, *Phys. Rev. Lett.* **2019**, *123*, 116104.
[5] J. Wang, L. Shi, J. Zi, *Phys. Rev. Lett.* **2022**, *129*, 236101.
[6] Y. Guo, M. Xiao, Y. Zhou, S. Fan, *Adv. Opt. Mater.* **2019**, *7*, 1801453.
[7] S. Kruk, B. Hopkins, I. I. Kravchenko, A. Miroshnichenko, D. N. Neshev, Y. S. Kivshar, *Apl Photon.* **2016**, *1*, 030801.
[8] E. W. Wang, T. Phan, S.-J. Yu, S. Dhuey, J. A. Fan, *Proc. Natl. Acad. Sci.* **2022**, *119*, e2122085119.
[9] C.-C. Chang, Z. Zhao, D. Li, A. J. Taylor, S. Fan, H.-T. Chen, *Phys. Rev. Lett.* **2019**, *123*, 237401.
[10] Y. Guo, M. Xiao, S. Fan, *Phys. Rev. Lett.* **2017**, *119*, 167401.
[11] V. Lousse, W. Suh, O. Kilic, S. Kim, O. Solgaard, S. Fan, *Opt. Express* **2004**, *12*, 1575.
[12] C. M. Lalau-Keraly, S. Bhargava, O. D. Miller, E. Yablonovitch, *Opt. Express* **2013**, *21*, 21693.
[13] M. Zhou, D. Liu, S. W. Belling, H. Cheng, M. A. Kats, S. Fan, M. L. Povinelli, Z. Yu, *ACS Photonics* **2021**, *8*, 2265.
[14] D. Sell, J. Yang, S. Doshay, J. A. Fan, *Adv. Opt. Mater.* **2017**, *5*, 1700645.
[15] J. Jiang, J. A. Fan, *Nano Lett.* **2019**, *19*, 5366.
[16] W. Ma, F. Cheng, Y. Xu, Q. Wen, Y. Liu, *Adv. Mater.* **2019**, *31*, 1901111.
[17] J. Lu, J. Vučković, *Opt. Express* **2012**, *20*, 7221.
[18] J. Lu, J. Vučković, *Opt. Express* **2013**, *21*, 13351.
[19] W. Ma, Y. Xu, B. Xiong, L. Deng, R.-W. Peng, M. Wang, Y. Liu, *Adv. Mater.* **2022**, *34*, 2110022.
[20] Z. Lin, C. Roques-Carmes, R. Pestourie, M. Soljačić, A. Majumdar, S. G. Johnson, *Nanophotonics* **2020**, *10*, 1177.
[21] F. Callewaert, V. Velev, P. Kumar, A. Sahakian, K. Aydin, *Sci. Rep.* **2018**, *8*, 1358.
[22] J. S. Jensen, O. Sigmund, *Laser Photonics Rev.* **2011**, *5*, 308.
[23] O. D. Miller, *Photonic design: From fundamental solar cell physics to computational inverse design*, University of California, Berkeley **2012**.
[24] R. H. Byrd, P. Lu, J. Nocedal, C. Zhu, *SIAM J. Sci. Comput.* **1995**, *16*, 1190.
[25] F. Wang, B. S. Lazarov, O. Sigmund, *Struct. Multidiscipl. Optim.* **2011**, *43*, 767.
[26] M. Zhou, B. S. Lazarov, F. Wang, O. Sigmund, *Comput. Methods Appl. Mech. Eng.* **2015**, *293*, 266.